Journal of Bioscience and Bioengineering
VOL. 132 No. 3, 310–320, 2021

www.elsevier.com/locate/jbiosc

Dependence of mitochondrial function on the filamentous actin cytoskeleton in cultured mesenchymal stem cells treated with cytochalasin B

Ágnes Kocsis,[1] Markus Pasztorek,[1] Eva Rossmanith,[1] Zoran Djinovic,[2] Torsten Mayr,[3] Sarah Spitz,[4] Helene Zirath,[4] Peter Ertl,[4] and Michael B. Fischer[1,5,*]

Department for Biomedical Research, Center of Experimental Medicine, Danube University Krems, Dr.-Karl-Dorrek-Straße 30, Krems an der Donau 3500, Austria,[1] ACMIT Gmbh (Austrian Center for Medical Innovation and Technology), Viktor Kaplan-Straße 2/1, Wiener Neustadt 2700, Austria,[2] Institute of Analytical Chemistry and Food Chemistry, Graz University of Technology, Stremayrgasse 9 / II + III, Graz 8010, Austria,[3] Faculty of Technical Chemistry, Institute of Applied Synthetic Chemistry and Institute of Chemical Technologies and Analytics, Vienna University of Technology, Getreidemarkt 9/163, Vienna 1060, Austria,[4] and Clinic for Blood Group Serology and Transfusion Medicine, Medical University of Vienna, Währinger Gürtel 18-20, Vienna 1090, Austria[5]

Received 4 March 2021; accepted 31 May 2021
Available online 24 June 2021

Owing to their self-renewal and multi-lineage differentiation capability, mesenchymal stem cells (MSCs) hold enormous potential in regenerative medicine. A prerequisite for a successful MSC therapy is the rigorous investigation of their function after *in vitro* cultivation. Damages introduced to mitochondria during cultivation adversely affect MSCs function and can determine their fate. While it has been shown that microtubules and vimentin intermediate filaments are important for mitochondrial dynamics and active mitochondrial transport within the cytoplasm of MSCs, the role of filamentous actin in this process has not been fully understood yet. To gain a deeper understanding of the interdependence between mitochondrial function and the cytoskeleton, we applied cytochalasin B to disturb the filamentous actin-based cytoskeleton of MSCs. In this study we combined conventional functional assays with a state-of-the-art oxygen sensor-integrated microfluidic device to investigate mitochondrial function. We demonstrated that cytochalasin B treatment at a dose of 16 μM led to a decrease in cell viability with high mitochondrial membrane potential, increased oxygen consumption rate, disturbed fusion and fission balance, nuclear extrusion and perinuclear accumulation of mitochondria. Treatment of MSCs for 48 h ultimately led to nuclear fragmentation, and activation of the intrinsic pathway of apoptotic cell death. Importantly, we could show that mitochondrial function of MSCs can efficiently recover from the damage to the filamentous actin-based cytoskeleton over a period of 24 h. As a result of our study, a causative connection between the filamentous actin-based cytoskeleton and mitochondrial dynamics was demonstrated.

[**Key words:** Mesenchymal stem cell; Actin cytoskeleton; Mitochondrial function; Cytochalasin B; Microfluidics; Oxygen sensor]

Mesenchymal stem cells (MSCs) hold enormous potential for the treatment of degenerative diseases and subsequent inflammatory conditions, owing to their self-renewal and multi-lineage differentiation capability (1–5). MSCs can repair connective tissue and organs by (i) integration and differentiation into the required tissue-specific mature cells at the target area (1–5), (ii) releasing their secretome (1–5), (iii) shedding subcellular fragments within the disease milieu (1–5) and (iv) donating mitochondria that are transferred to damaged cells via tunneling nanotubes in their immediate surrounding (6,7). A prerequisite for a successful MSC therapy is a rigorous investigation of their function after *in vitro* cultivation and expansion. It is important to note, that the therapeutical potential of cell culture expanded human MSCs is adversely affected by the age of the donor, the cultivation conditions, the selection of medium supplements and the numbers of passages, leading to a senescence-mediated loss of function (8,9).

Mitochondria are essential for physiological MSC function as they are the power plants of the cell and in addition to energy generation, they participate in calcium signaling, redox homeostasis and apoptosis (10). Mitochondria are responsive to microenvironmental cues, change shape rapidly and move in the cytoplasm to areas with high adenosine triphosphate (ATP) demand (11). Mitochondrial dysfunction leads to changes in mitochondrial morphology as a result of altered fusion and fission dynamics, network formation and perinuclear accumulation (12,13). Non-functional mitochondria or mitochondria exhibiting altered mitochondrial membrane potential (MMP) are readily degraded by mitophagy through ubiquitin (Ub)-dependent and Ub-independent receptor pathways (14–16). This intrinsic cellular process of mitochondrial quality surveillance prevents the occurrence of MSCs damage by initiating the intrinsic death pathway, involving initiator caspase 9 and executioner caspases 3/6/7, resulting in apoptosis (17–19). Therefore, damages introduced to mitochondria during the process of *in vitro* cultivation adversely affect MSCs function and determines their fate.

* Corresponding author at: Department for Biomedical Research, Center of Experimental Medicine, Danube University Krems, Dr. Karl Dorrek Strasse 30, Krems an der Donau 3500, Austria.
E-mail address: michael.fischer@donau-uni.ac.at (M.B. Fischer).

1389-1723/$ – see front matter
https://doi.org/10.1016/j.jbiosc.2021.05.010

Another important but overlooked aspect limiting MSCs functionality is associated with the well-established and cost-efficient *in vitro* cultivation technique to adhere MSCs on plastic surfaces. This technique, however, induces the formation of intracellular stress fibers (SFs) that change the physical properties of MSCs including cell shape, inner tension, cell motility and deformability (20). Intracellular SFs are contractile actin bundles that transmit forces across focal adhesions to the surrounding extracellular matrix (ECM) network, and in a reciprocal manner, the ECM can influence the actin filament formation of adherent MSCs (21–23). These tensile forces control MSCs shape and regulate the balance between differentiation and death (24–26). We could previously show that the cultivation of MSCs in adherence to plastic surfaces using commercially available growth media, led to increased SF formation, where bold filamentous actin bundles spanned the entire length of MSCs (20). Serum substitution with human platelet lysate partially reversed this effect in two dimensional (2D) cultivated MSCs leading to lower levels of total actin protein and more delicate SF formation (20). The importance of the actin cytoskeleton for the generation of inner forces within cells has been described extensively (21–26), but the role of the actin filament network for mitochondrial function in cultured MSCs remains unclear. Mitochondria are mechano-responsive to the effects of forces set up in the interior of MSCs by SFs, where high tensile forces negatively influence mitochondrial fusion and fission dynamics and alter the accumulation and distribution of mitochondria in the cytoplasm (13). The role of cytoskeletal structures, such as microtubules and vimentin intermediate filaments in the mitochondrial movement in the cytoplasm as well as in the active fusion and fission dynamics is essential (27–30), but it seems likely that actin filaments are also important contributors of mitochondrial function (29,30).

For a successful therapeutic application of MSCs in a clinical setting, therapists need to understand the complex regulatory pathways connecting MSCs cytoarchitecture with mitochondrial function. In this paper, we investigated the dependence of mitochondrial function on the actin-based cytoskeleton in 2D cultured amnion-derived MSCs. We used cytochalasin B (CB) to disturb the filamentous actin-based cytoarchitecture of MSCs in a precisely regulated manner. The efficiency of cytochalasins in the inhibition of actin polymerization, especially of CB, was investigated extensively in tumor cell lines but rarely in primary cells like MSCs (19,31–34). We investigated the potential changes in MMP, the abnormalities in mitochondrial network formation and distribution within the cytoplasm, as well as the initiation of the intrinsic death pathway and the extent of nuclear extrusion as a consequence of actin disruption-induced mitochondrial damage in CB-treated adherent MSC cultures. To complete our investigations on the mitochondrial function we analyzed the oxygen consumption rate of CB-treated MSCs in a state-of-the-art optical sensor-integrated microfluidic device, enabling both dynamic cultivation as well as the non-invasive monitoring of cellular respiratory activity (35,36). Oxygen is essential to aerobic respiration, while it is the terminal electron acceptor of the mitochondrial electron transport chain, which transfers electrons from high energy metabolites to drive ATP production (10,11). The oxygen consumption rate reflects the oxygen, consumed through aerobic respiration within a defined artificial microenvironment of the microfluidic device and gives a direct measure of the metabolic status of cultured MSCs. Finally, we investigated the potential of MSCs to recover from CB-induced filamentous actin network disruption and the subsequent mitochondrial damage. Self-renewal and differentiation are the essential characteristics of MSCs intended for therapeutic applications (1–5), therefore the recovery of mitochondrial function after the disruption of the filamentous actin network might be a predictor of positive treatment outcome.

MATERIALS AND METHODS

Isolation, culturing and characterization of amnion-derived MSCs The placenta was obtained from healthy delivering women in accordance with the Austrian Hospital Act (KAG 1982) after a written informed consent was signed according to the criteria established following the recommendations given by the ethic commissions. Studies, involving human participants were reviewed and approved by EK791/2008, EK1192/2015 and GS1-EK-4/3,122,015. MSCs were isolated from the amnion membrane of the placenta as described previously (37,38). Isolated stromal cells from the amnion were cultured as single cells in a 5% CO_2 humidified incubator (Stericycle, Thermo Fisher Scientific, Waltham, MA, USA) at 37°C in adherence to plastic surfaces (in T25 cell culture treated flasks, Nunc, Thermo Fisher Scientific), a protocol recommended by the International Society for Cellular Therapy (ISCT) (39). To omit differentiation of MSCs along the mesenchymal lineage, cells were grown in MSCBM basal medium supplemented with MSCGM SingleQuots (both from Lonza, Basel, Switzerland), 100 U/mL penicillin, 100 μg/mL streptomycin and 250 ng/mL amphotericin B (all from Gibco, Thermo Fisher Scientific). Culture medium was changed regularly every 3–4 days and cells were harvested when they reached a confluency of 80%. Amnion-derived stromal cells were characterized for the expression of the MSC-specific markers ecto-5′-nucleotidase (CD73-APC), Thy-1, a glycophosphatidyl-inositol anchored conserved cell surface protein (CD90-FITC), and endoglin, a component of the receptor complex of TGF-β (CD105-PE-Dy7, all from eBioscience, Thermo Fisher Scientific in concentrations recommended by the company) by flow cytometry using the CytoFLEX flow cytometer (Beckman Coulter, Krefeld, Germany). To exclude the effect of unspecific binding, isotype specific control mAbs (eBioscience, Thermo Fisher Scientific) were used and amnion-derived cells positive for all the MSC-specific markers were considered MSCs (39). For the consistence of all experiments, only MSCs of passage 1 were used.

Cytochalasin B treatment CB (Sigma–Aldrich, St. Louis, MO, USA) was dissolved in dimethyl sulfoxide (DMSO, Sigma–Aldrich) to a 2000 μM stock solution. To reach the desired working solutions the stock solution was further diluted in MSCGM complete medium to the final concentration of 0.5–128 μM and MSCs were incubated at 37°C in 5% CO_2 humidified environment for the time indicated. After the treatments, MSCs were washed with phosphate buffered saline (PBS) before the indicated measurements were carried out. The recovery potential of MSCs after 3 or 24 h of CB treatment was accessed after another 24 h of cultivation with fresh MSCGM complete medium.

Fluorometric assays to assess cell viability MSCs were seeded in a density of 10,000 MSCs/well within 96-well plates (Greiner Bio-One, Kremsmünster, Austria) in triplicates using the MSCGM complete medium and cultivated for 24 h at 37°C in 5% CO_2 humidified environment. MSCs were then treated with CB in different concentrations ranging from 0.5 to 128 μM for either 3 or 24 h. Viability of MSCs was investigated using 10% PrestoBlue HS Cell Viability Reagent (Invitrogen, Thermo Fisher Scientific) in MSCGM. MSCs were incubated with PrestoBlue in the dark for 4 h at 37°C in 5% CO_2 humidified environment. The recovery potential was assessed 24 h after cessation of treatment. A multimode plate reader (Synergy, BioTek, Winooski, VT, USA) was used to access the fluorescence intensity.

Flow cytometric analysis to measure mitochondrial membrane potential and mitochondrial volume For mitochondrial studies, MSCs were seeded in 24-well plates (Greiner Bio-One) in a density of 20,000 MSCs/well in duplicates. After 24 h of cultivation, MSCs were treated with 16 μM of CB for either 3 or 24 h and the recovery potential of MSCs was measured 24 h after cessation of treatment. The membrane potential analysis was performed by using tetramethylrhodamine ethyl ester (TMRE, 25 nM, Sigma–Aldrich) as previously described (40,41). The stock solution was diluted in MSCGM and the detached MSCs were stained for 15 min at room temperature in the dark and analyzed thereafter by flow cytometry investigating up to 25,000 MSCs. To quantify mitochondria, MSCs were stained for 30 min at 37°C using MitoTracker Green FM (100 nM, Molecular Probes, Thermo Fisher Scientific) and MSC viability was analyzed by a live/dead (L/D) assay (Invitrogen, Thermo Fisher Scientific). Measurements were carried out using the CytoFLEX and data were analyzed by FlowJo (Becton Dickinson, Franklin Lakes, NJ, USA).

Confocal laser scanning microscopy to investigate mitochondrial membrane potential, mitochondrial network, the initiation of the intrinsic pathway of apoptotic cell death and nuclear extrusion MSCs were seeded as triplicates in chamber slides (8 chamber Nunc Lab-Tek II, Thermo Fisher Scientific) in a density of 5000 cells/chamber and cultivated for 24 h. MSCs were fixed with fixation and permeabilization solution (eBioscience, Thermo Fisher Scientific) and incubated with Phalloidin AF-488 (0.1 U/mL, Molecular Probes, Thermo Fisher Scientific) to reveal actin, followed by MitoTracker Red CMX Ros (100 nM,

Molecular Probes, Thermo Fisher Scientific) to stain mitochondria, and DAPI (Sigma–Aldrich) to highlight nuclei. Serial dilutions of Phalloidin AF-488 and MitoTracker Red CMX Ros were tested to assure separation of the fluorescent signals and optimize fluorophore concentration to preclude self-quenching (20). The probes were mounted with Fluoromount-G (Southern Biotechnology, Thermo Fisher Scientific) and analyzed with an alpha Plan-Apochromat 63x objective and a Leica TCS SP8 confocal microscope (Leica, Wetzlar, Germany). For live cell imaging of mitochondrial membrane potential, MSCs were seeded in high-quality glass-bottom chambers (μ-slide, 8 well, high, Ibidi, Gräfelfing, Germany) and were stained with TMRE for 30 min, washed with PBS and analyzed by confocal microscopy. MSCs were treated either for 3 h or for 24 h with 16 μM CB and recovery was investigated 24 h after cessation of treatment. Images obtained by confocal microscopy (resolution: 2048 × 2048 pixels) were analyzed by ImageJ-Fiji and mitochondrial network was further analyzed by the Mitochondria Analyzer plugin according to the recommendations (42,43). For measurements along the Z-axis, stack images were made by confocal microscopy with 0.33 μm slice thickness (Nyquist-optimized) and stacks were analyzed by ImageJ-Fiji. To investigate the initiation of the intrinsic pathway of apoptotic cell death, MSCs were seeded in chamber slides (8 chamber Nunc Lab-Tek II) in a density of 5000 MSCs/chamber and cultured for 24 h in 37°C in 5% CO_2 humidified environment. MSCs were treated with 16 μM CB either for 24 h or for 48 h. Thereafter MSCs were fixed and permeabilized and subsequently incubated for 4 h with monoclonal antibodies specific to either caspase 9 (2 μg mouse mAb/mL, cone F-10) or caspase 3 (2 μg mouse mAb/mL, cone E–8, both from Santa Cruz Biotechnology, Dallas, TX, USA). Slides were than incubated with a polyclonal goat anti-mouse Ig labeled with either AF-488 (3 mg/mL) to reveal caspase 9 or with AF-594 (3 mg/mL, both from Jackson Laboratories, Bar Harbor, MN, USA) to highlight caspase 3. Finally, nuclei were stained with DAPI (Sigma–Aldrich). All probes were mounted with Fluoromount-G™ and investigations were carried out with an alpha Plan-Apochromat 63x objective and confocal microscopy. Image analysis was performed using ImageJ-Fiji.

A non-invasive, real-time, optical sensor-integrated microfluidic device to monitor partial oxygen pressure Microfluidic chips were fabricated with integrated optical sensor spots made of oxygen-sensitive microparticles, following previously developed protocols (Fig. 1A and B). Microfluidic chips were comprised of two glass substrates (VWR, Thermo Fisher Scientific) bonded together with medical adhesive films (ARcare 8259 and ARseal 90,880, Adhesive Research, Limerick, Ireland) and holes with a diameter of 0.8 mm were drilled into the upper glass substrate for the microfluidic connectors (35). The sensor spots were deposited on the upper glass slide prior to the assembly of the microfluidic device and the characterization and calibration of the oxygen sensor spots were performed as described previously (36). The channel dimensions were initially optimized to the large size of MSCs, since MSCs in solution have a size of 50–60 μm when measured by flow cytometry and can flatten out during cultivation in adherence to collagen spanning more than 100 μm in diameter. The geometry of the channels was designed using a CAD software (AutoCAD 2019, Autodesk, San Rafael, CA, USA) and was optimized to achieve a total length of 18.5 mm and a width of 3 mm to favor MSCs cultivation. The structure of the channels was cut into the adhesive films with a desktop vinyl cutter (GS-24 Desktop Cutter, Roland DGA, Willich, Germany). Three layers of adhesive films were used to obtain a chamber height of 0.45 mm. The volume of one channel was 15 μL and the seeding area was 0.33 cm^2 to approximate the surface area of a 96-well plate well. Tygon tubes of 5 mm length (LMT-55, Ismatec, IDEX Health & Science, Wertheim, Germany) were glued (Loctite Hysol 9492, Henkel, Düsseldorf, Germany) on the top glass substrate as inlet and outlet

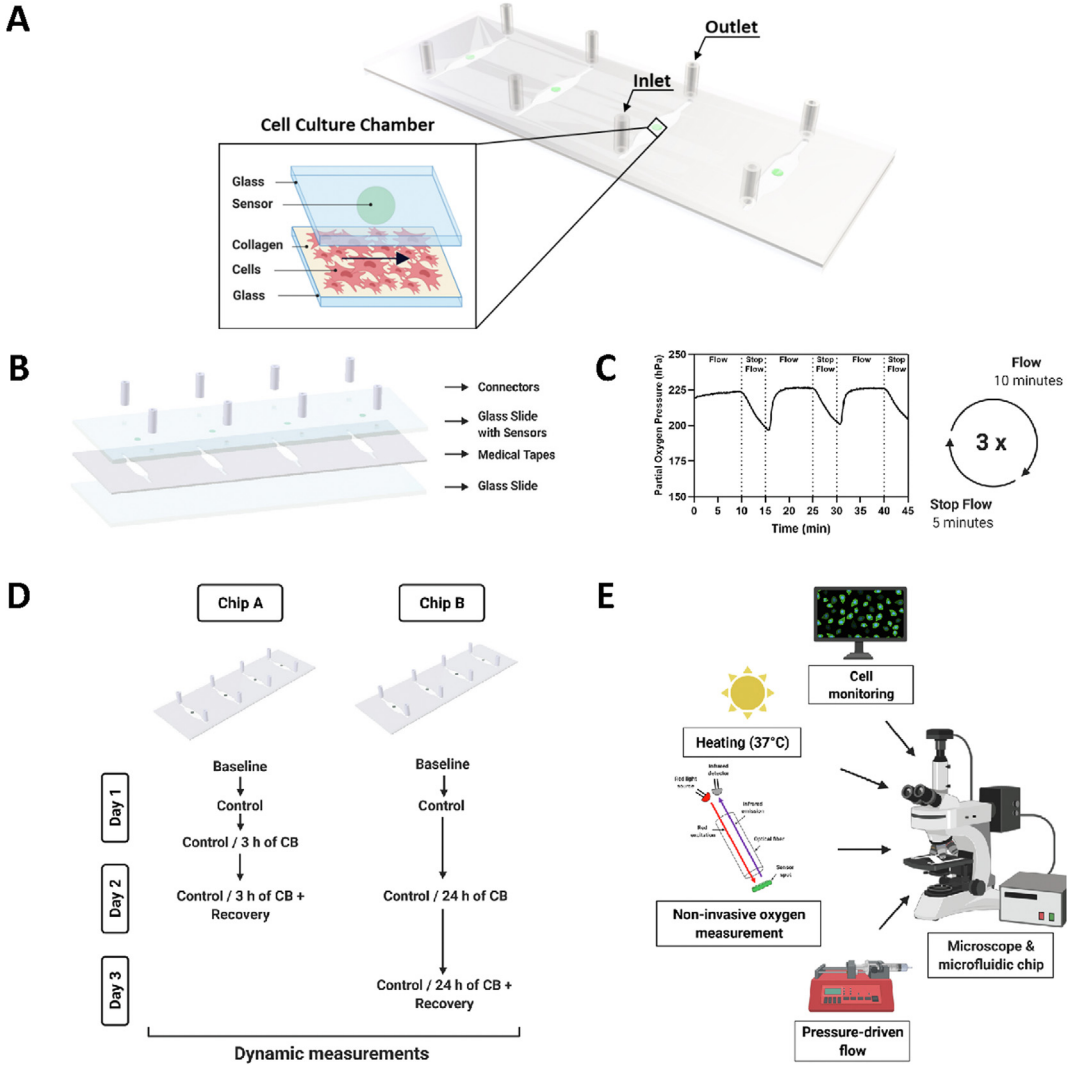

FIG. 1. Microfluidic platform to measure partial oxygen pressure. (A) Design of the microfluidic device with a cubic intersection presenting the microfluidic MSC culture. (B) Fabrication steps of the device. (C) Dynamic flow protocol of the oxygen consumption rate measurements. (D) Protocols of the 16 μM CB treatment of MSCs for 3 and 24 h with the subsequent 24 h recovery phases. (E) Experimental setup of the oxygen consumption rate measurements.

connectors for the microfluidic tubing. The microfluidic setup was assembled on a heated microscope plate (ThermoPlate Tokai Hit, Shizuoka, Japan) to secure a stable 37°C environment for the functional investigations of MSCs (Fig. 1E). Microfluidic devices were sterilized with UV light and thereafter coated with 1% collagen type I (Sigma–Aldrich) for 1 h at 37°C. MSCs were seeded in an initial density of 5000 cells/channel in MSCGM supplemented with 0.5% HEPES (Sigma–Aldrich) and cultivated for 24 h before the measurements to allow approximately 80% confluency. The partial oxygen pressure in the channels was assessed by non-invasive optical fiber sensing technology (FireSting, PyroScience, Aachen, Germany) before seeding, after 24 h of cultivation, and after treatment with 16 μM CB for either 3 or 24 h. The recovery phase was set to 24 h (Fig. 1D). One of the four channels of the microfluidic devices was designated as internal control and images of adherent MSCs were taken before and after each measurement (Fig. 2B). To obtain a reference value an initial oxygen measurement was performed before MSCs were seeded into the channels. A flow-stop flow regime was applied as previously described by Zirath et al. (35) to access the oxygen consumption rate of MSCs under dynamic conditions (Fig. 1C). The dissolved oxygen level in the chambers was saturated during the 10 min of 10 μL/min flow period. The oxygen depletion in the chambers was registered during the 5 min of stop flow period. Three cycles of flow and stop flow measurements were performed sequentially, and the obtained amplitude gave the oxygen consumption measured in ΔhPa. The oxygen consumption rate (ΔhPa/min) was then calculated as ΔhPa divided by the duration of the stop flow measurement sequence. To compensate the incidental deviations in the initial seeding number, the number of MSCs per mm^2 was calculated for each channel before the initiation of the first experiment, after 24 h of cultivation and the measured oxygen consumption values were normalized to 10,000 cells. The results of the upcoming experiments were proportionated to these normalized values.

Statistical analysis Results were expressed as mean ± standard deviation (SD) unless stated otherwise and error bars on all figures represent SD. Mann–Whitney *U*-test or unpaired *t*-test was performed for unpaired analysis while paired *t*-test or Wilcoxon test was applied for paired analysis. When more than two groups were analyzed, one-way ANOVA or Kruskal–Wallis tests were performed for unpaired analysis. For multiple comparison, the adequate post hoc test was applied to identify the exact position of the statistical difference. Statistical analysis was performed by GraphPad Prism 8.0 (GraphPad Software, San Diego, CA, USA) and results were considered statistically significant when $p < 0.05$.

RESULTS

Dose-dependent decrease in MSC viability after cytochalasin B treatment and their recovery potential Initial CB toxicity studies were conducted to identify the 50% inhibitory concentration (IC_{50}) in cultured MSCs of passage 1, expressing the MSC-specific markers CD73, CD90 and CD105 (Fig. S1) (39). When adherent MSCs were treated with increasing concentrations of CB ranging from 0.5 to 128 μM for either 3 or 24 h, we observed

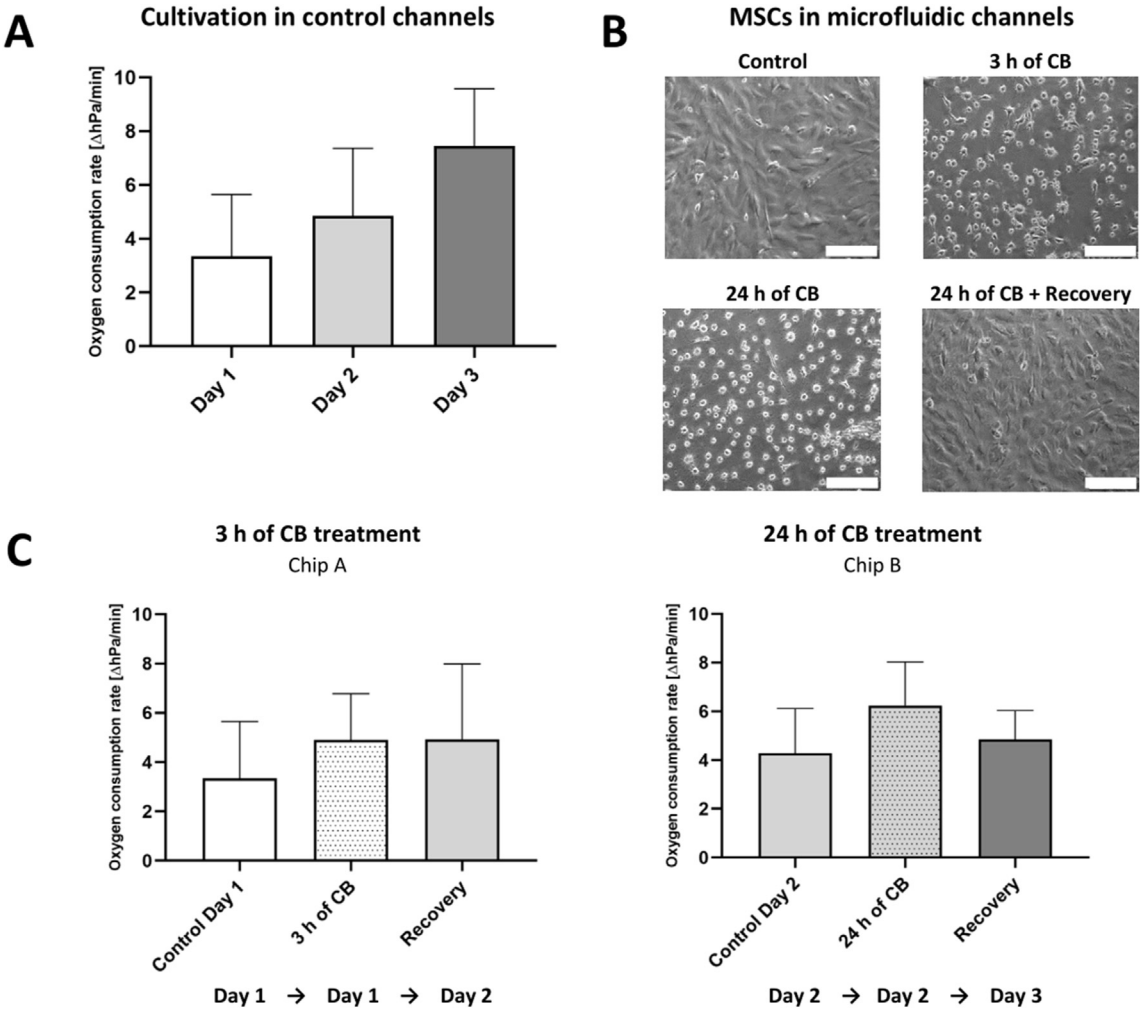

FIG. 2. Oxygen consumption rate. (A) Measurement of the oxygen consumption rate of control MSCs in microfluidic cultures over a period of 3 days (n = 5). (B) Images of microfluidic cultures before and after the 16 μM CB treatment for 3 and 24 h and after the 24 h recovery phase subsequent to the 24 h CB treatment as investigated by phase contrast microscopy (10× magnification, scale bar: 200 μm). (C) Left, oxygen consumption rates of control MSCs and after the 16 μM CB treatment for 3 and after the 24 h recovery phase (n = 5, Mann–Whitney and Wilcoxon tests). Right, oxygen consumption rates of control MSCs and after the 16 μM CB treatment for 3 and after the 24 h recovery phase (n = 5, Mann–Whitney and Wilcoxon tests). Results are expressed as mean ± SD.

a dose-dependent decrease in cell viability (Fig. 3A, left and B, left). At a concentration of 32 μM CB, approximately 50% of the MSCs were dead after 24 h of treatment (IC_{50}), increasing to 75% when 128 μM CB was used (Fig. 3B, left). Short term CB treatment of MSCs for 3 h, although dose-dependent, showed only a moderate effect with 40% dead MSCs at the highest concentration of 128 μM CB (Fig. 3A, left).

To investigate whether the damage introduced to the actin cytoskeleton of CB-treated MSCs is reversible, we established a two-stage treatment and recovery/relapse protocol. The follow-up measurements indicated the proliferation and the recovery or relapse of MSCs 24 h after the correspondent CB treatments. The change in the mean fluorescent intensity (MFI) was calculated as a percentage of the measured metabolic activity of MSCs after the 24 h recovery phase and of MSCs after the initial CB treatment and was termed recovery or relapse according to the direction of the change. When the recovery potential of MSCs was investigated after 3 or 24 h of CB treatment, recovery was detected after treatment with concentrations up to 32 μM (IC_{50}) (Fig. 3A, right and B, right). No sign of recovery was found in MSCs treated with 64 μM and relapse was found only in MSCs treated with 128 μM CB for 24 h (Fig. 3B, right). As a result of our cell culture optimization and CB toxicity study, an initial treatment for 3 or 24 h with 16 μM CB accompanied by a 24 h recovery phase after the 24 h CB treatment

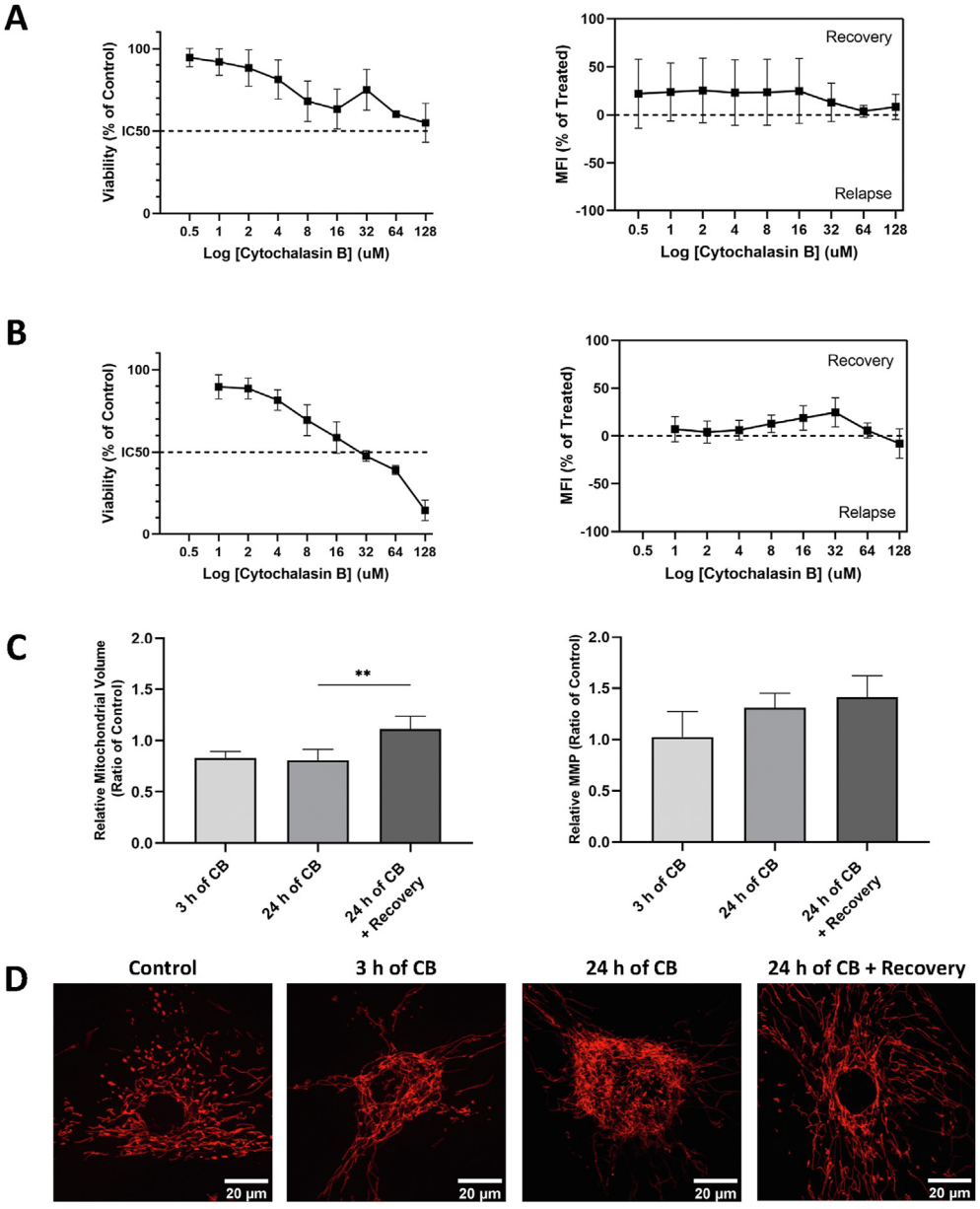

FIG. 3. Viability, mitochondrial membrane potential (MMP) and mitochondrial volume. MSCs were treated with 0.5–128 μM CB viability was determined subsequently by a fluorometric assay using PrestoBlue. Recovery or relapse of MSCs were measured 24 h after the cessation of CB treatment. (A) Left, viability after CB treatment for 3 h (n = 13). Right, mean fluorescent intensity (MFI) compared to treated, measured 24 h after the cessation of the 3 h CB treatment (n = 8). (B) Left, viability after CB treatment for 24 h (n = 6). Right, MFI compared to treated, measured 24 h after the cessation of the 24 h CB treatment (n = 6). Results are expressed as mean ± SD. (C) Relative mitochondrial volume and MMP are given in comparison to controls after 3 and 24 h of the 16 μM CB treatment and 24 h after the cessation of the 24 h CB treatment. Mitochondria were stained with MitoTracker green and MMP with TMRE and MSCs were analyzed by flow cytometry. Results are expressed as mean ± SD (n = 5, Kruskal–Wallis and Wilcoxon tests, $^{**}p < 0.01$). Left: Relative mitochondrial volume. Right: Relative MMP. (D) Images of single MSCs, stained with TMRE (red), before and after the 3 and 24 h of 16 μM CB treatment and 24 h after the cessation of the 24 h CB treatment (later referred as 24 h recovery phase) as investigated by confocal microscopy.

was selected for all subsequent experiments, since this was the concentration one log step under the IC_{50} (~32 μM) value.

Increased mitochondrial membrane potential and decreased mitochondrial footprint and volume in cytochalasin B-treated MSCs Two indicators of mitochondrial function, MMP and mitochondrial volume were measured by TMRE or MitoTracker staining and flow cytometry in cultured MSCs before and after CB treatment and after recovery. The TMRE assay could give evidence on disturbed MMP as a consequence of mitochondrial disorder induced by CB treatment. Here we segregated the TMRE positive MSCs population to MSCs with lower or higher MMP (Fig. S2). We further investigated the changes in average MMP of living MSCs with higher MMP after CB treatment and recovery (Fig. 3C, right). Of note, during CB treatment and after recovery, MMP dynamics followed cell viability, in particular, higher MMP fraction resembles higher MSC viability (Fig. S2B). We observed that within the population of MSCs, the fraction of cells with higher MMP decreases after treatment of 16 μM CB, an effect detected as early as after 3 h, with a tendency to decrease further when treated for up to 24 h (Fig. S2). MSCs with lower MMP conversely increased (Fig. S2). When MSCs had the chance to recover after the 24 h treatment with CB, the numbers of MSCs with higher MMP increased (Fig. S2), indicating a high recovery potential under these circumstances. Interestingly, the average MMP of MSCs increased after 24 h of CB treatment and during the recovery phase but remained unaltered after 3 h of CB treatment (Fig. 3C, right). MMP alterations during CB treatment and after recovery were observable through live cell confocal microscopy as well (Fig. 3D). The flow cytometric MitoTracker assay provided evidence on decreased mitochondrial volume induced by CB treatment and increased mitochondrial volume during the subsequent recovery phase (Figs. 3C, left and S3).

Mitochondrial network formation, perinuclear accumulation of mitochondria and nuclear extrusion in MSCs after cytochalasin B treatment Mitochondrial volume, fusion and fission dynamics that give rise to mitochondrial morphology, as well as the perinuclear accumulation of mitochondria are additional aspects of mitochondrial function. Measurements at the middle cross section and along the Z-axis were performed to determine the mitochondrial footprint and volume as well as the mitochondrial distribution in MSCs. Mitochondrial morphology is described by the number of punctuates, rods and mitochondrial networks in the cell (Fig. 4B). Here we demonstrated that cross-sectional mitochondrial density, determined by the mitochondrial footprint and the number of punctuates and rods decreased (Fig. 4C and E), while mean mitochondrial rod length (including rods as well as networks) and subsequently network formation increased during CB treatment (Fig. 4E). The mitochondrial footprint and the number of punctuates and rods, in contrast, increased during recovery (Fig. 4B and E), while mitochondrial rod length and network formation decreased (Fig. 4E), indicating that the effect of CB treatment is partially reversible. Since mitochondrial location within the cytoplasm is connected with high ATP demand on site, assessing the organelles distribution is an important aspect in mitochondrial studies. When the fusion and fission dynamics of mitochondria are functionally intact as seen in untreated MSCs, the mitochondrial appearance in MSCs would favor loose network formation and rods (Figs. 3D and 4A). Damage to the mitochondria, as observed after CB treatment, led to (i) increased mitochondrial fusion rate and subsequently to network formation and (ii) to mitochondrial condensation around the nucleus, a so-called perinuclear accumulation. We found very condensed networks in the perinuclear area in MSCs even after treatment for 3 h with CB as determined by confocal laser scanning microscopy (Figs. 3D and 4A). When MSCs recovered after CB treatment, the perinuclear accumulation of mitochondria reversed to a loose network formation (Figs. 3D and 4A). Measurements along the Z-axis of MSCs were carried out to determine the mitochondrial volume and mitochondrial volume distribution (Figs. 4D and S4). We found slight decrease in the mitochondrial volume upon CB treatment and a moderate increase after the 24 h recovery phase (Fig. S4A), however, we found no significant change in the cell height (Fig. S4B). When we compared the mitochondrial volume to the total cell volume we found an increase upon CB treatment and a decrease after recovery (Fig. 4D). Mitochondria along the Z-axis was accumulated around the central cross section of the cell before CB treatment and after recovery and was more evenly distributed along the height of MSCs upon CB treatment (Fig. S4C and D).

Furthermore, we investigated whether there is a causative connection between the actin cytoskeletal disruption induced by CB treatment and the resulting impairment in mitochondrial network, size of nucleus and nuclear extrusion (Figs. 5, S5 and S6). According to the results of the nuclear extrusion and perinuclear accumulation measurements, we set up grades from 1 to 5 to scale the effect of actin cytoskeletal disruption on the above-mentioned parameters. Grade 1 resembles unaffected MSCs with high cell viability and intact MSC function with minor perinuclear accumulation of mitochondria and no nuclear extrusion, while grade 5 resembles perinuclear accumulation of mitochondria, irreversible mitochondrial damage and increased nuclear extrusion as a result of extensive cell damage (Fig. 5A). We found a treatment time-dependent increase of cells with higher grades in CB-treated MSCs. Interestingly, the 24 h recovery phase after treatment could not totally reverse this effect in MSCs (Fig. 5B). For the image analysis of the perinuclear accumulation of mitochondria by ImageJ-Fiji, the radius of the nucleus (R) was determined first, then the perinuclear radius (1.5 R) was calculated accordingly, as described before (Fig. 5A, schematic of grade 1) (44). Here we could show that CB treatment led to the expected actin depolymerization (Fig. 5C, left) and subsequently to a decrease in the size of nucleus (Fig. 5C, right), perinuclear accumulation of mitochondria (Fig. 5D, left) and nuclear extrusion (Fig. 5D, right), an effect that was partially reversible during recovery.

Nuclear translocation of initiator caspase 9 and executioner caspase 3 in cytochalasin B-treated MSCs Here we investigated whether damages to mitochondrial function could induce the initiation of the intrinsic pathway of apoptotic cell death. This pathway is activated when damaged mitochondria cannot be removed efficiently by mitophagy and cytochrome C gets released from the damaged mitochondria to the cytosol where it forms the apoptosome with APAF-1. The apoptosome then recruits and activates initiator caspase 9 that in turn activates executioner caspase 3, resulting in apoptosis (17–19). A previous study indicated that caspases translocate to the nucleus during apoptosis (17). Here we could show that 24 and 48 h of 16 μM CB treatment induced a certain nuclear translocation of caspase 9/3 in MSCs (Fig. 6A) while the total amount of caspase 9/3 decreased (Fig. 6B). The amount of nuclear caspase 9 increased significantly upon treatment even after 24 h (Fig. 6A, left), while the amount of nuclear caspase 3 presented only a moderate increase after 48 h of treatment accompanied by nuclear fragmentation (Figs. 5A, grade 5 and 6A, right). Here we provided evidence for the active transfer of caspase 9 from the cytoplasm to the nucleus even after 24 h of 16 μM CB treatment (Fig. 6A, left).

Increased oxygen consumption rate in MSCs after cytochalasin B treatment Oxygen consumption rate is another important parameter of mitochondrial function. Here a non-invasive optical sensor-integrated microfluidic device was fabricated containing oxygen-sensitive microparticle-based

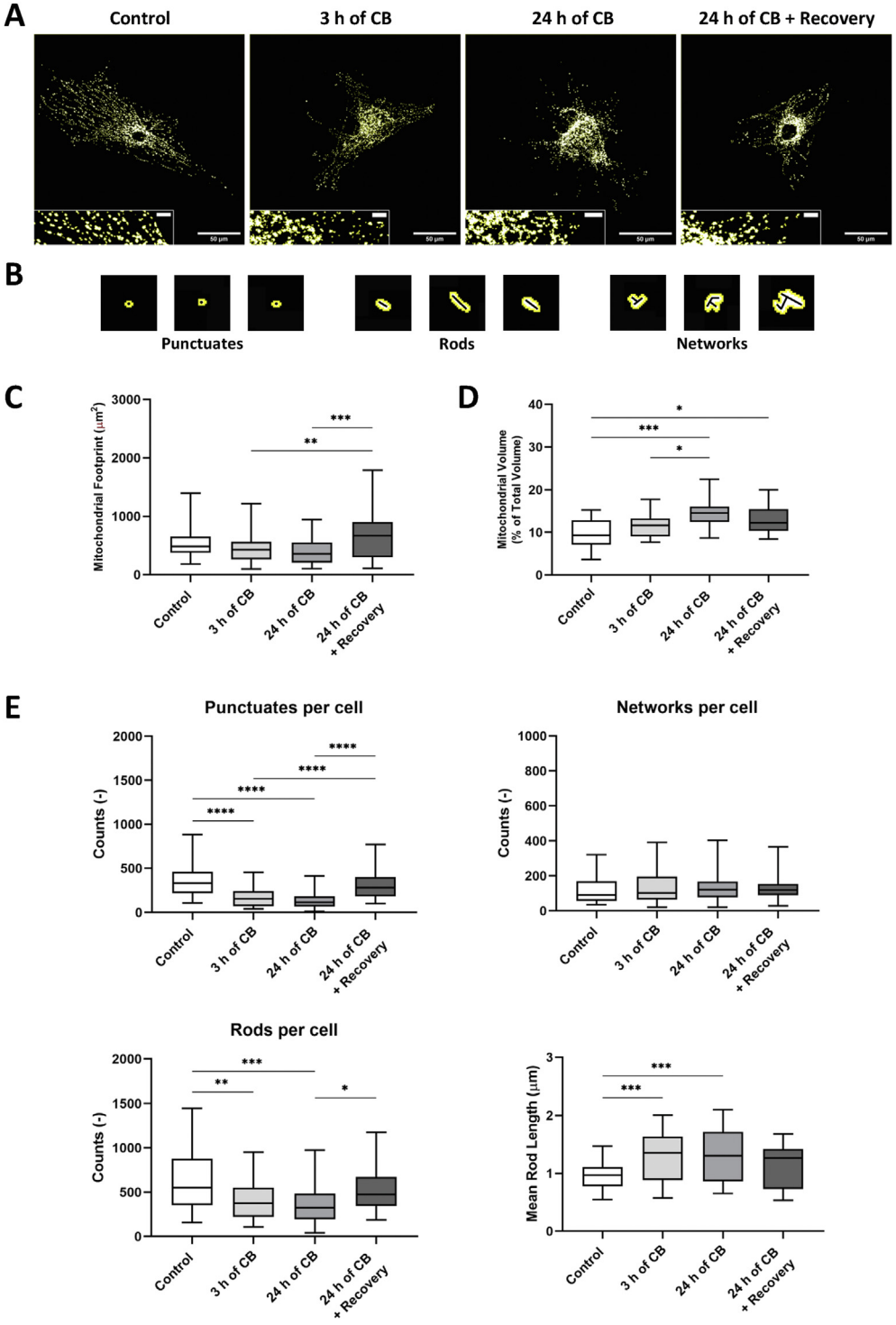

FIG. 4. Mitochondrial network analysis. (A) Mitochondrial pattern of MSCs before and after the 3 and 24 h of 16 μM CB treatment and after the 24 h recovery phase as investigated by confocal microscopy and analyzed by Mitochondria Analyzer. A representative part of the mitochondrial network is shown in the inserts (scale bar: 5 μm). Mitochondria were stained with MitoTracker (here in white and yellow). (B) Representative images of individual mitochondrial structures such as punctuates, rods and networks from Mitochondria Analyzer. (C) Mitochondrial footprints in μm^2 per cell (n = 45, ordinary one-way ANOVA, $^{**}p < 0.01$ and $^{***}p < 0.001$). (D) Mitochondrial volume as the percentage of total cell volume (n = 20, ordinary one-way ANOVA, $^{*}p < 0.05$ and $^{***}p < 0.001$). (E) Numbers of mitochondrial punctuates, rods and networks per cell and mean rod length of mitochondrial network in μm per cell before and after the 3 and 24 h of 16 μM CB treatment and after the 24 h recovery phase (n = 45, ordinary one-way ANOVA, $^{*}p < 0.05$, $^{**}p < 0.01$, $^{***}p < 0.001$ and $^{****}p < 0.0001$). Data are represented as box plot diagrams.

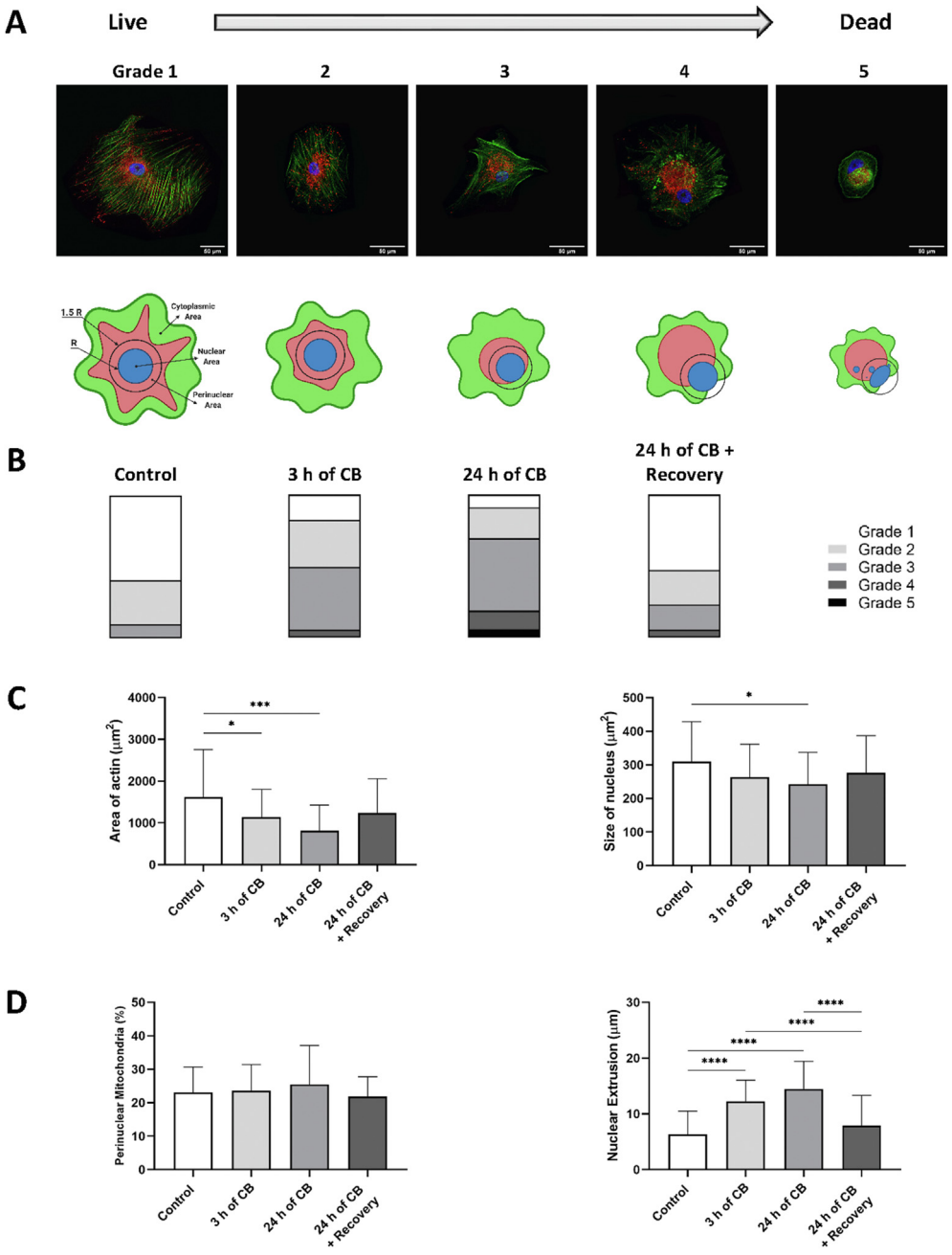

FIG. 5. Effects of CB treatment on the filamentous actin cytoskeleton, nucleus and perinuclear accumulation of mitochondria. (A) Images of single MSCs were graded from 1 to 5 in the severity of perinuclear accumulation of mitochondria and nuclear extrusion. Filamentous actin was stained with Phalloidin (green), mitochondria with MitoTracker (red) and nuclei with DAPI (blue) and investigated by confocal microscopy and analyzed by ImageJ-Fiji. (B) Incidence of grades before and after the 3 and 24 h of 16 µM CB treatment and after the 24 h recovery phase. (C) Left, area of filamentous actin in μm^2 per cell. Right, size of the nucleus in μm^2 per cell. Results are expressed as mean ± SD (n = 45, ordinary one-way ANOVA, $^{*}p < 0.05$ and $^{***}p < 0.001$). (D) Left, perinuclear accumulation of mitochondria given as percentage of total mitochondria per cell. Righ, extent of nuclear extrusion in µm per cell. Results are expressed as mean ± SD (n = 45, ordinary one-way ANOVA, $^{****}p < 0.0001$).

sensors for the time-resolved monitoring of the partial oxygen pressure within the microchannels (Fig. 1A). The microfluidic oxygen measurement platform was set up on a heated microscope plate enabling the simultaneous monitoring of microfluidic MSC cultures (Fig. 2B). Oxygen consumption rate increased over time, dependent on the increase in cell number due to proliferation of MSCs in the channels of the microfluidic devices. The 2 days doubling time of the MSCs population were observable according to our results (Fig. 2A). We detected an increase in oxygen consumption rate of cultured MSCs after 3 h as well as after 24 h of CB treatment compared to the control channels of the same chips with the untreated MSCs (Fig. 2A and C). When MSCs recovered under dynamic conditions, the oxygen consumption rate of the previously CB-treated MSCs for 3 h was almost the same as of untreated MSCs in control channels after the corresponding 2 days of proliferation (Fig. 2A and C, left). In the population previously treated for 24 h with CB, however, the oxygen consumption rate decreased after the recovery phase compared to the untreated MSCs after the corresponding 3 days of proliferation (Fig. 2A and C, right).

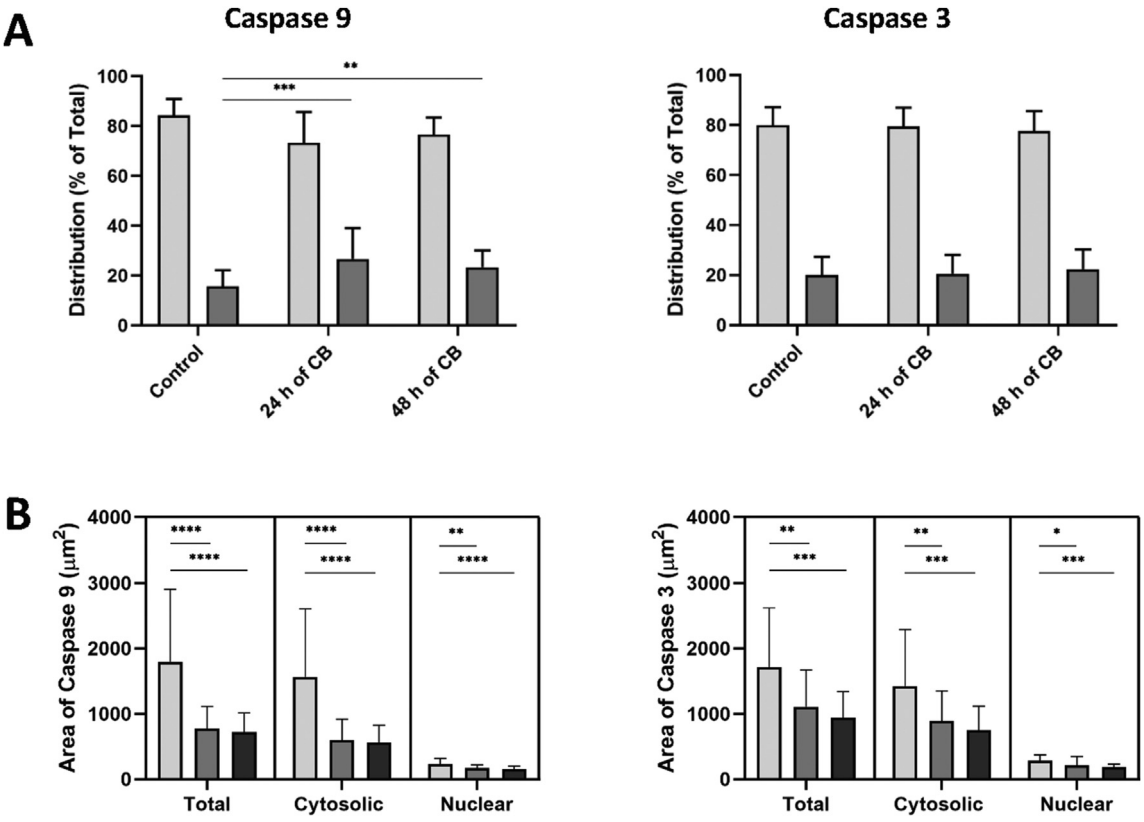

FIG. 6. Nuclear translocation analysis and semi-quantification of initiator caspase 9 and executioner caspase 3. Cytoplasmic or nuclear localization and semi-quantification of caspase 9/3 in MSCs before and after the 16 μM CB treatment for 24 h and 48 h, as investigated by confocal microscopy and analyzed by ImageJ-Fiji. (A) Left, localization of caspase 9. Right, localization of caspase 3 (nuclear caspases in dark and cytoplasmic localization in light gray, n = 25, ordinary one-way ANOVA, $^{**}p < 0.01$ and $^{***}p < 0.001$). (B) Left: Semi-quantification of caspase 9 in the cytoplasm and in the nucleus. Right, semi-quantification of caspase 3 in the cytoplasm and in the nucleus. Results are expressed as mean ± SD (control in light gray, 24 h of CB treatment in dark gray and 48 h of CB treatment in black, n = 25, ordinary one-way ANOVA, $^{**}p < 0.01$, $^{***}p < 0.001$ and $^{****}p < 0.0001$).

DISCUSSION

During the process of cultivation, it is highly relevant to preserve MSC function when these cells are used in a clinical setting (1–9). MSCs are extremely sensitive to signals regulating the cytoskeleton, including actin filament formation, and can express mechano-sensitive receptors that are responsive to physical changes and external force application (21–26). Mitochondria, the power plants of the cell, are essential for physiological MSC function, can change shape rapidly and can move in the cytoplasm to areas with high ATP demand (10,11). Microtubules and vimentin intermediate filaments are important for mitochondrial function (27–30), but the role of actin filaments in this process is not entirely clear (29,30). The *in vitro* cultivation technique to adhere MSCs on plastic surfaces affects the cytoskeleton and induces the formation of intracellular actin bundles (stress fibers) (20). It was shown previously that CB can inhibit actin filament network formation (21–26,31,32) and binds covalently to mammalian glucose transporter proteins (33,34), which affect crucial cell functions.

Here we applied CB to investigate the dependence of mitochondrial function in cultured MSCs in relation to a precisely regulated actin filament disintegration. Therefore, we investigated mitochondrial damage and recovery by changes in cell viability, MMP and oxygen consumption and alterations in the mitochondrial network, as well as the extent of nuclear extrusion and the initiation of the intrinsic death pathway by the nuclear translocation of the caspase 9/3 in cultured MSCs as a consequence of CB treatment. We treated cultured MSCs with increasing concentrations (0.5–128 μM) of CB for either 3 or 24 h that caused a dose-dependent inhibition of actin filament formation and a decrease in cell viability. We found an increased amount of total MMP within living MSCs and a decreased MSC population with higher MMP when cells were treated with 16 μM of CB for 3 or 24 h, an effect that was partially reversible during the 24 h recovery phase. Following the treatment of MSCs with CB the mitochondrial footprint and volume decreased while the mean mitochondrial rod length increased. These effects after 24 h of CB treatment were accompanied by perinuclear accumulation of mitochondria, significant nuclear extrusion and translocation of initiator caspase 9 that after 48 h resulted in a moderate nuclear translocation of executioner caspase 3 and nuclear fragmentation as signs of apoptosis. MSCs treated with up to 32 μM of CB showed a decent recovery potential with the potential to restore mitochondrial activity and dynamics to almost normal levels. High concentrations of more than 32 μM of CB or 48 h of 16 μM CB treatment, however, resulted in irreversible cellular damage.

Mitochondrial fusion and fission dynamics that give rise to mitochondrial morphology and perinuclear accumulation of mitochondria determines mitochondrial function (12,13). When MSCs suffer from damage by CB treatment the number of mitochondria will decrease by a process called mitophagy where damaged mitochondria with low MMP get endocytosed and dismantled by subsequent lysosomal degradation (14–16). Here we revealed a decrease of mitochondrial footprint and volume after CB treatment and an increase during the recovery phase. Due to the shrinkage of MSCs upon CB treatment, however, reversable changes in the mitochondrial accumulation could be observed. The mitochondrial

volume of CB-treated MSCs compared to the total cell volume increases and the distribution of the mitochondrial mass is more even along the Z-axis upon CB treatment. Furthermore, it is of utmost importance whether the fusion and fission dynamics of mitochondria are disturbed and where mitochondria are located within the cytoplasm, because mitochondria move actively to the area of the highest ATP consumption (10,11). When the fusion and fission dynamics of mitochondria are functionally intact as observed in untreated MSCs, the mitochondrial structure would favor loose network formation. Solid damage to the mitochondria led to increased rate of fusion thus solid network formation and perinuclear accumulation of mitochondria. It was previously shown that an increased fusion rate results in increased MMP and reactive oxygen species (ROS) production that is associated with the perinuclear accumulation of mitochondria (12–14).

Furthermore, the intrinsic pathway of cell death, initiated by the release of cytochrome C from the mitochondria into the cytoplasm, activates the initiator caspase 9 to setup the apoptosome comprising of adapter proteins such as APAF-1 (18). The apoptosome complex can then further activate the executioner caspases 3/6/7 that translocate to the nucleus and facilitate nuclear fragmentation and DNA cleavage (17). This endpoint of the death pathway determines the fate of MSCs by apoptosis. Here we demonstrated that 24 h of 16 μM CB treatment induced a significant increase in the translocation of initiator caspase 9 from the cytoplasm to the nucleus. It was shown previously that the initiator caspase 9 can participate in the proteolysis of nuclear components after translocation to the nucleus and interact with components of the apoptosome complex (16). Interestingly, the executioner caspases 3 showed only moderate dynamics in CB-treated MSCs as the ratio of nuclear caspase 3 increased only slightly even after 48 h of treatment. Nuclear fragmentation, alongside with caspase 3 nuclear translocation, was observable only after 48 h of 16 μM CB treatment, indicating that the initiation of apoptosis, thus irreversible cell damage occurs only after this timepoint.

Another major indicator of mitochondrial function is mitochondrial respiration that determines MSC fate both *in vivo* as well as *in vitro* and relies on oxygen (45–47). Oxygen concentration, however, can vary throughout the human body ranging from approximately 14% in the lung and in the circulation and can oscillate within physiological levels of 0.5–5% in cartilage and stem cell niches within bone marrow. In the stem cell niches, although richly vascularized, the partial oxygen concentration in the blood of bone marrow vessels is relatively low when compared to blood in other tissues (48–50). Despite the different demand of oxygen in specific tissues, cultivation of human MSCs was conducted predominantly under atmospheric oxygen concentration of 21% and this hyperoxia also could lead to a higher stress sensibility due to the more intense mitochondrial respiration. Here we demonstrated that oxygen consumption rate of cultured MSCs after 16 μM CB treatment increased under dynamic conditions. The reason of the increased respiration rate lies within the glucose inhibitory effect of CB (34). Due to low levels of glucose available in CB-treated MSCs, cells favor aerobic glycolysis and potentially consuming more oxygen to provide sufficient ATP (51). In healthy MSCs and following recovery, however, glycolysis and mitochondrial metabolism is balanced and mitochondrial respiration decreases, especially the electron transport chain responsible for formation of ROS, resulting in reduced risk of DNA, RNA, lipid and protein damage (52). Increased oxygen consumption and MMP was also observed previously in tumor cell lines following a low-dose CB treatment that provided evidence for a respiratory compensation mechanism, called Warburg effect, against the glycose inhibitory effect of CB (34,53). It is important to note that permanent increase in mitochondrial respiration caused by a long-term CB treatment results in the initiation of the intrinsic death pathway due to irreversible mitochondrial damage caused by the excessive ROS production (52).

The recovery potential of CB-treated MSCs was assessed 24 h after the cessation of the treatment. The recovery of MSCs after the 3 h of CB treatment was fully functional with a high cell viability and an unaltered oxygen consumption rate, indicating no permanent damage to the mitochondria. There was a decrease in oxygen consumption rate, however, during the recovery phase of MSCs previously treated with CB for 24 h, indicating irreversible mitochondrial damage. The results provide evidence for an increased oxygen consumption, MMP and fusion rate, perinuclear mitochondrial accumulation and nuclear extrusion even after a short-term CB treatment, however, MSCs were able to recover their mitochondrial function during the 24 h recovery phase.

An advantage of our approach is the use of MSCs that are stem cells of the connective tissue with unique therapeutic potential (1–5). In this paper, we combined conventional and self-developed functional assays with a state-of-the-art, fiber optic, sensor-integrated microfluidic device to investigate mitochondrial function after the disintegration of the filamentous actin cytoskeleton of MSCs by CB and during recovery. A causative connection between actin cytoskeletal disruption and impairment in mitochondrial network and respiration was demonstrated in cultured MSCs treated with CB using this combined approach. Furthermore, disassembly of the actin filament network and the resulting impairments of the mitochondrial function led to the initiation of the intrinsic pathway of cell death and the resulting nuclear defragmentation after long-term CB treatment. We found a clear dependence of mitochondrial function on the presence of an intact actin filament network in cultured MSCs. MSCs, however, were robust to correct moderate damages to the actin filament network introduced by CB, during the 24 h recovery phase that would otherwise lead to serious damage to MSC function. The interdependence of the actin cytoskeleton and mitochondrial functions suggests the need to monitor the actin SF formation and the mitochondrial activity in *in vitro* cultured adherent MSCs intended for clinical use.

Supplementary data to this article can be found online at https://doi.org/10.1016/j.jbiosc.2021.05.010.

ACKNOWLEDGMENTS

This work was supported by the NÖ Forschungs- und Bildungsges.m.b.H. (grant number N F+B LS15-004) and the government of Lower Austria, Department of Economics, Tourism and Technology (WST3) (grant number WST3-F-5030664/009-2018) and co-financed by the European Regional Development Fund (grant numbers INTERREG ATCZ 133 and 215). The authors thank the CEO of Austrian Center for Medical Innovation and Technology (ACMIT Gmbh) Nikolaus Dellantoni for financial support, the Austrian Cluster for Tissue Regeneration (ACTR) headed by Prof. DI Dr. Heinz Redl for networking and Dominik Rabl from the Graz University of Technology for the preparation of the oxygen sensitive sensor spots.

References

1. **Sagaradze, G. D., Basalova, N. A., Efimenko, A. Y., and Tkachuk, V. A.:** Mesenchymal stromal cells as critical contributors to tissue regeneration, Front. Cell Dev. Biol., **8**, 576176 (2020).
2. **Shammaa, R., El-Kadiry, A. E., Abusarah, J., and Rafei, M.:** Mesenchymal stem cells beyond regenerative medicine, Front. Cell Dev. Biol., **8**, 72 (2020).
3. **Noel, D., Djouad, F., Bouffi, C., Mrugala, D., and Jorgensen, C.:** Multipotent mesenchymal stromal cells and immune tolerance, Leuk. Lymphoma, **48**, 1283–1289 (2007).
4. **Shi, M., Liu, Z. W., and Wang, F. S.:** Immunomodulatory properties and therapeutic application of mesenchymal stem cells, Clin. Exp. Immunol., **164**, 1–8 (2011).

5. **Wu, X., Jiang, J., Gu, Z., Zhang, J., Chen, Y., and Liu, X.:** Mesenchymal stromal cell therapies: immunomodulatory properties and clinical progress, Stem Cell Res. Ther., **11**, 345 (2020).
6. **Jackson, M. V. and Krasnodembskaya, A. D.:** Analysis of mitochondrial transfer in direct co-cultures of human monocyte-derived macrophages (MDM) and mesenchymal stem cells (MSC), Bio Protoc., **7**, e2255 (2017).
7. **Li, C., Cheung, M. K. H., Han, S., Zhang, Z., Chen, L., Chen, J., Zeng, H., and Qiu, J.:** Mesenchymal stem cells and their mitochondrial transfer: a double-edged sword, Biosci. Rep., **39**, BSR20182417 (2019).
8. **Wang, Y., Liu, Y., Chen, E., and Pan, Z.:** The role of mitochondrial dysfunction in mesenchymal stem cell senescence, Cell Tissue Res., **382**, 457–462 (2020).
9. **Banimohamad-Shotorbani, B., Kahroba, H., Sadeghzadeh, H., Wilson, D. M., 3rd, Maadi, H., Samadi, N., Hejazi, M. S., Farajpour, H., Onari, B. N., and Sadeghi, M. R.:** DNA damage repair response in mesenchymal stromal cells: from cellular senescence and aging to apoptosis and differentiation ability, Ageing Res. Rev., **62**, 101125 (2020).
10. **McBride, H. M., Neuspiel, M., and Wasiak, S.:** Mitochondria: more than just a powerhouse, Curr. Biol., **16**, R551–R560 (2006).
11. **Newmeyer, D. D. and Ferguson-Miller, S.:** Mitochondria: releasing power for life and unleashing the machineries of death, Cell, **112**, 481–490 (2003).
12. **Kudryavtseva, A. V., Krasnov, G. S., Dmitriev, A. A., Alekseev, B. Y., Kardymon, O. L., Sardinia, A. F., Fedorova, M. S., Pokrovsky, A. V., Melnikova, N. V., Kaprin, A. D., Moskalev, A. A., and Snezhkina, A. V.:** Mitochondrial dysfunction and oxidative stress in aging and cancer, Oncotarget, **7**, 44879–44905 (2016).
13. **Sebastian, D., Palacin, M., and Zorzano, A.:** Mitochondrial dynamics: coupling mitochondrial fitness with healthy aging, Trends Mol. Med., **23**, 201–215 (2017).
14. **Bravo-San Pedro, J. M., Kroemer, G., and Galluzzi, L.:** Autophagy and mitophagy in cardiovascular disease, Circ. Res., **120**, 1812–1824 (2017).
15. **Sulkshane, P., Ram, J., and Glickman, M. H.:** Ubiquitination of intramitochondrial proteins: implications for metabolic adaptability, Biomolecules, **10**, 1559 (2020).
16. **Xie, Y., Liu, J., Kang, R., and Tang, D.:** Mitophagy receptors in tumor biology, Front. Cell Dev. Biol., **8**, 594203 (2020).
17. **Prokhorova, E. A., Kopeina, G. S., Lavrik, I. N., and Zhivotovsky, B.:** Apoptosis regulation by subcellular relocation of caspases, Sci. Rep., **8**, 12199 (2018).
18. **Kulms, D., Dussmann, H., Poppelmann, B., Stander, S., Schwarz, A., and Schwarz, T.:** Apoptosis induced by disruption of the actin cytoskeleton is mediated via activation of CD95 (Fas/APO-1), Cell Death Differ., **9**, 598–608 (2002).
19. **Hwang, J., Yi, M., Zhang, X., Xu, Y., Jung, J. H., and Kim, D. K.:** Cytochalasin B induces apoptosis through the mitochondrial apoptotic pathway in HeLa human cervical carcinoma cells, Oncol. Rep., **30**, 1929–1935 (2013).
20. **Pasztorek, M., Rossmanith, E., Mayr, C., Hauser, F., Jacak, J., Ebner, A., Weber, V., and Fischer, M. B.:** Influence of platelet lysate on 2D and 3D amniotic mesenchymal stem cell cultures, Front. Bioeng. Biotechnol., **7**, 338 (2019).
21. **Atherton, P., Stutchbury, B., Jethwa, D., and Ballestrem, C.:** Mechanosensitive components of integrin adhesions: role of vinculin, Exp. Cell Res., **343**, 21–27 (2016).
22. **Bays, J. L., Peng, X., Tolbert, C. E., Guilluy, C., Angell, A. E., Pan, Y., Superfine, R., Burridge, K., and DeMali, K. A.:** Vinculin phosphorylation differentially regulates mechanotransduction at cell-cell and cell-matrix adhesions, J. Cell Biol., **205**, 251–263 (2014).
23. **Zeiger, A. S., Loe, F. C., Li, R., Raghunath, M., and Van Vliet, K. J.:** Macromolecular crowding directs extracellular matrix organization and mesenchymal stem cell behavior, PloS One, **7**, e37904 (2012).
24. **Holle, A. W., Tang, X., Vijayraghavan, D., Vincent, L. G., Fuhrmann, A., Choi, Y. S., del Alamo, J. C., and Engler, A. J.:** In situ mechanotransduction via vinculin regulates stem cell differentiation, Stem Cell, **31**, 2467–2477 (2013).
25. **Yang, C., DelRio, F. W., Ma, H., Killaars, A. R., Basta, L. P., Kyburz, K. A., and Anseth, K. S.:** Spatially patterned matrix elasticity directs stem cell fate, Proc. Natl. Acad. Sci. USA, **113**, E4439–E4445 (2016).
26. **Zhou, Y., Chen, H., Li, H., and Wu, Y.:** 3D culture increases pluripotent gene expression in mesenchymal stem cells through relaxation of cytoskeleton tension, J. Cell. Mol. Med., **21**, 1073–1084 (2017).
27. **Heggeness, M. H., Simon, M., and Singer, S. J.:** Association of mitochondria with microtubules in cultured cells, Proc. Natl. Acad. Sci. USA, **75**, 3863–3866 (1978).
28. **Biskou, O., Casanova, V., Hooper, K. M., Kemp, S., Wright, G. P., Satsangi, J., Barlow, P. G., and Stevens, C.:** The type III intermediate filament vimentin regulates organelle distribution and modulates autophagy, PloS One, **14**, e0209665 (2019).
29. **Krendel, M., Sgourdas, G., and Bonder, E. M.:** Disassembly of actin filaments leads to increased rate and frequency of mitochondrial movement along microtubules, Cell Motil. Cytoskeleton, **40**, 368–378 (1998).
30. **Kandel, J., Angelin, A. A., Wallace, D. C., and Eckmann, D. M.:** Mitochondrial respiration is sensitive to cytoarchitectural breakdown, Integr. Biol. (Camb.), **8**, 1170–1182 (2016).
31. **MacLean-Fletcher, S. and Pollard, T. D.:** Mechanism of action of cytochalasin B on actin, Cell, **20**, 329–341 (1980).
32. **Cooper, J. A.:** Effects of cytochalasin and phalloidin on actin, J. Cell Biol., **105**, 1473–1478 (1987).
33. **Malaisse, W. J., Giroix, M. H., and Sener, A.:** Effect of cytochalasin B on glucose uptake, utilization, oxidation and insulinotropic action in tumoral insulin-producing cells, Cell Biochem. Funct., **5**, 183–187 (1987).
34. **Motrescu, E. R., Otto, A. M., Brischwein, M., Zahler, S., and Wolf, B.:** Dynamic analysis of metabolic effects of chloroacetaldehyde and cytochalasin B on tumor cells using bioelectronic sensor chips, J. Cancer Res. Clin. Oncol., **131**, 683–691 (2005).
35. **Zirath, H., Rothbauer, M., Spitz, S., Bachmann, B., Jordan, C., Muller, B., Ehgartner, J., Priglinger, E., Muhleder, S., Redl, H., and other 4 authors:** Every breath you take: non-invasive real-time oxygen biosensing in two- and three-dimensional microfluidic cell models, Front. Physiol., **9**, 815 (2018).
36. **Ehgartner, J., Sulzer, P., Burger, T., Kasjanow, A., Bouwes, D., Krühne, U., Klimant, I., and Mayr, T.:** Online analysis of oxygen inside silicon-glass microreactors with integrated optical sensors, Sens. Actuators B Chem., **228**, 748–757 (2016).
37. **Soncini, M., Vertua, E., Gibelli, L., Zorzi, F., Denegri, M., Albertini, A., Wengler, G. S., and Parolini, O.:** Isolation and characterization of mesenchymal cells from human fetal membranes, J. Tissue Eng. Regen. Med., **1**, 296–305 (2007).
38. **Rossmanith, E.:** Actin filaments and mitochondrial dynamics in response to platelet lysate cultivation of mesenchymal stem cells, in: Abstracts from the 45th ESAO congress, 12–15 September 2018, Madrid, Spain, Int. J. Artif. Organs, **41**, 614–615 (2018).
39. **Dominici, M., Le Blanc, K., Mueller, I., Slaper-Cortenbach, I., Marini, F., Krause, D., Deans, R., Keating, A., Prockop, D., and Horwitz, E.:** Minimal criteria for defining multipotent mesenchymal stromal cells. The international society for cellular therapy position statement, Cytotherapy, **8**, 315–317 (2006).
40. **Rothbauer, M., Praisler, I., Docter, D., Stauber, R. H., and Ertl, P.:** Microfluidic impedimetric cell regeneration assay to monitor the enhanced cytotoxic effect of nanomaterial perfusion, Biosensors, **5**, 736–749 (2015).
41. **Crowley, L. C., Christensen, M. E., and Waterhouse, N. J.:** Measuring mitochondrial transmembrane potential by TMRE staining, Cold Spring Harb. Protoc., **2016**, https://doi.org/10.1101/pdb.prot087361 (2016).
42. **Legland, D., Arganda-Carreras, I., and Andrey, P.:** MorphoLibJ: integrated library and plugins for mathematical morphology with ImageJ, Bioinformatics, **32**, 3532–3534 (2016).
43. **Chaudhry, A.:** Mitochondria analyzer, manual, version 2.0.2. https://github.com/AhsenChaudhry/Mitochondria-Analyzer/blob/master/Mitochondria%20Analyzer%20Manual.pdf (2019)
44. **do Couto, N. F., Queiroz-Oliveira, T., Horta, M. F., Castro-Gomes, T., and Andrade, L. O.:** Measuring intracellular vesicle density and dispersion using fluorescence microscopy and ImageJ/FIJI, Bio Protoc., **10**, e3703 (2020).
45. **Mohyeldin, A., Garzon-Muvdi, T., and Quinones-Hinojosa, A.:** Oxygen in stem cell biology: a critical component of the stem cell niche, Cell Stem Cell, **7**, 150–161 (2010).
46. **Fabian, Z.:** The effects of hypoxia on the immune-modulatory properties of bone marrow-derived mesenchymal stromal cells, Stem Cells Int., **2019**, 2509606 (2019).
47. **Watts, D., Gaete, D., Rodriguez, D., Hoogewijs, D., Rauner, M., Sormendi, S., and Wielockx, B.:** Hypoxia pathway proteins are master regulators of erythropoiesis, Int. J. Mol. Sci., **21**, 8131 (2020).
48. **Wagner, B. A., Venkataraman, S., and Buettner, G. R.:** The rate of oxygen utilization by cells, Free Radic. Biol. Med., **51**, 700–712 (2011).
49. **Gille, J. J. and Joenje, H.:** Cell culture models for oxidative stress: superoxide and hydrogen peroxide versus normobaric hyperoxia, Mutat. Res., **275**, 405–414 (1992).
50. **Jagannathan, L., Cuddapah, S., and Costa, M.:** Oxidative stress under ambient and physiological oxygen tension in tissue culture, Curr. Pharmacol. Rep., **2**, 64–72 (2016).
51. **Dai, Z., Shestov, A. A., Lai, L., and Locasale, J. W.:** A flux balance of glucose metabolism clarifies the requirements of the Warburg effect, Biophys. J., **111**, 1088–1100 (2016).
52. **Klaunig, J. E., Wang, Z., Pu, X., and Zhou, S.:** Oxidative stress and oxidative damage in chemical carcinogenesis, Toxicol. Appl. Pharmacol., **254**, 86–99 (2011).
53. **Hrynevich, S. V., Pekun, T. G., Waseem, T. V., and Fedorovich, S. V.:** Influence of glucose deprivation on membrane potentials of plasma membranes, mitochondria and synaptic vesicles in rat brain synaptosomes, Neurochem. Res., **40**, 1188–1196 (2015).